JACS
JOURNAL OF THE AMERICAN CHEMICAL SOCIETY
pubs.acs.org/JACS
Article

Bright and Stable Light-Emitting Diodes Based on Perovskite Quantum Dots in Perovskite Matrix

Yuan Liu,[⊥] Yitong Dong,[⊥] Tong Zhu, Dongxin Ma, Andrew Proppe, Bin Chen, Chao Zheng, Yi Hou, Seungjin Lee, Bin Sun, Eui Hyuk Jung, Fanglong Yuan, Ya-kun Wang, Laxmi Kishore Sagar, Sjoerd Hoogland, F. Pelayo García de Arquer, Min-Jae Choi, Kamalpreet Singh, Shana O. Kelley, Oleksandr Voznyy, Zheng-Hong Lu, and Edward H. Sargent*

Cite This: https://doi.org/10.1021/jacs.1c02148

ABSTRACT: Light-emitting diodes (LEDs) based on metal halide perovskite quantum dots (QDs) have achieved impressive external quantum efficiencies; however, the lack of surface protection of QDs, combined with efficiency droop, decreases device operating lifetime at brightnesses of interest. The epitaxial incorporation of QDs within a semiconducting shell provides surface passivation and exciton confinement. Achieving this goal in the case of perovskite QDs remains an unsolved challenge in view of the materials' chemical instability. Here, we report perovskite QDs that remain stable in a thin layer of precursor solution of perovskite, and we use strained QDs as nucleation centers to drive the homogeneous crystallization of a perovskite matrix. Type-I band alignment ensures that the QDs are charge acceptors and radiative emitters. The new materials show suppressed Auger bi-excition recombination and bright luminescence at high excitation (600 W cm^{-2}), whereas control materials exhibit severe bleaching. Primary red LEDs based on the new materials show an external quantum efficiency of 18%, and these retain high performance to brightnesses exceeding 4700 cd m^{-2}. The new materials enable LEDs having an operating half-life of 2400 h at an initial luminance of 100 cd m^{-2}, representing a 100-fold enhancement relative to the best primary red perovskite LEDs.

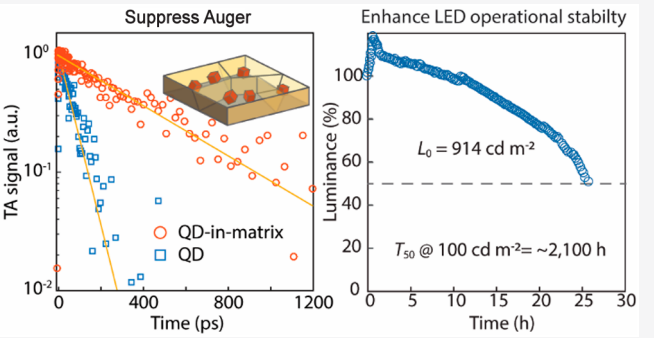

INTRODUCTION

Quantum confinement in perovskite QDs provides an approach to tune the band gap to a desired emission color while also increasing the exciton binding energy for a higher radiative rate.[1] Much progress has recently been seen in perovskite QD based LEDs.[2−4] However, the charge carriers in QDs can become trapped at surface defect sites, compromising luminescence efficiency as well as materials stability.[5,6]

Growing heteroepitaxial semiconducting shells address this problem in II-VI and III-V QDs.[7−9] Unfortunately, such core−shell structures have remained elusive in perovskite QDs, a result of their structural lability and of the dynamic nature of ligands as they bind to perovskite surfaces:[10,11] the solvents used to introduce shell precursors immediately redissolve the cores. Recent progress includes coating perovskite nanoparticles with insulators such as SiO_2 and Cs_4PbBr_6,[12,13] which can potentially improve the stability of QDs in devices, but which comes at the price of impeding charge transport.

Unlike covalently bonded semiconductors that require high temperatures for growth, perovskites have low formation energies and crystallize at moderate temperatures,[14] suggesting the potential for convenient near-room-temperature growth of a matrix. A matrix can protect the embedded luminophore and also reduce the carrier density in the material, thus suppressing unwanted Auger recombination. Building an efficient QD-in-matrix luminophore requires small lattice mismatch and type-I band alignment at the interface. As a matrix material, perovskites can be tuned in band gap and lattice spacing by mixing different halide anions in the crystal.[15]

Unfortunately, in bulk perovskites made using mixed-halide materials, inhomogeneous crystallization leads to a spatially dependent composition in crystal grains (Figure 1A,B). The energy landscape of a mixed-halide perovskite fluctuates, leading to wide emission line widths and reduced quantum yields of luminescence (Figure 1C). Additionally, upon photoexcitation and electrical excitation, this halide segregation

Received: February 24, 2021

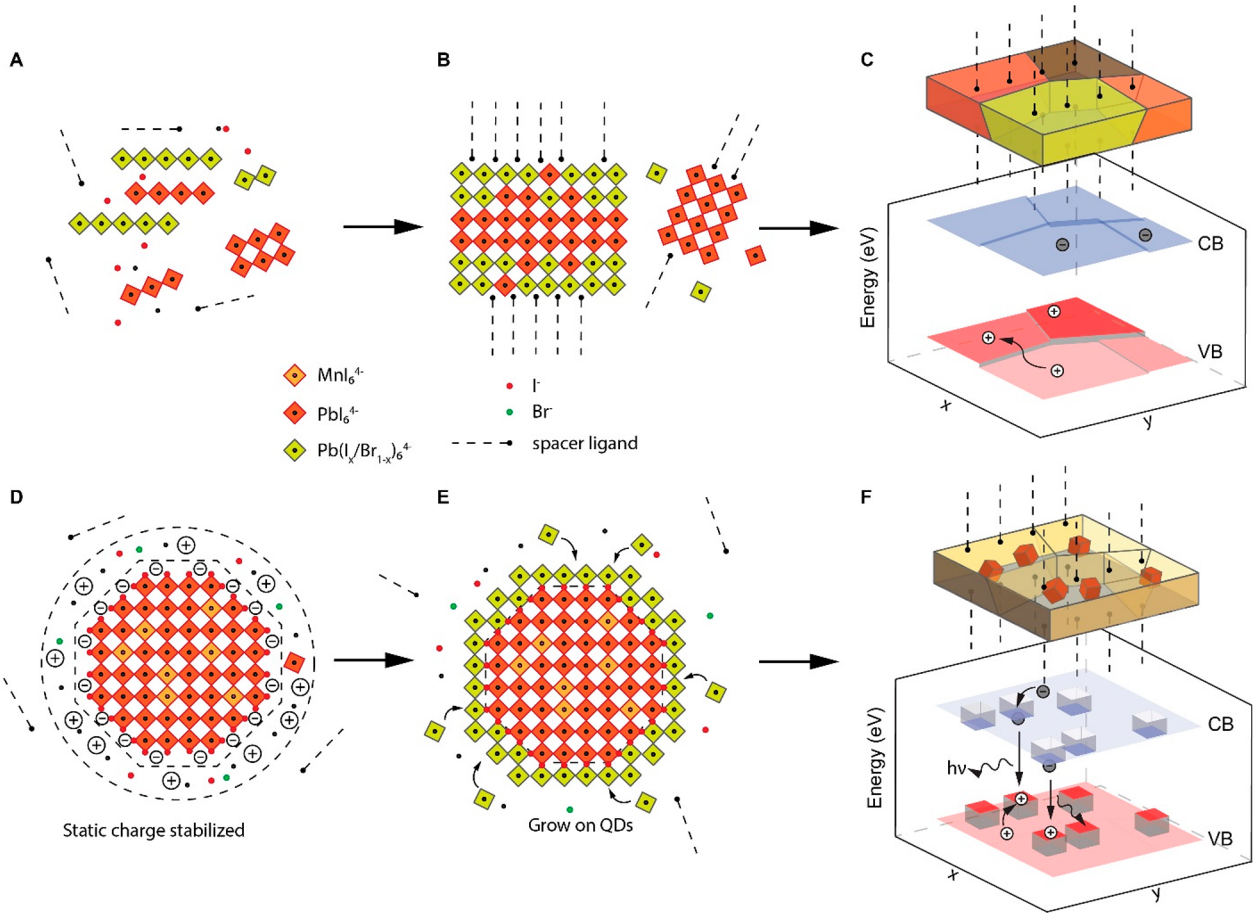

Figure 1. Crystallization and energy landscape of QD-in-matrix solids. (A) Perovskite precursor forms thin perovskite frameworks as nucleation centers. (B) Formation of low dimensional mixed-halide perovskites having inhomogeneous compositions. (C) Energy-level gradation in the matrix perovskite without QDs (CB: conduction band, VB: valence band). (D) Strain-tuned $CsPbI_3$ QDs protected using a bipolar shell following surface ligand treatment. (E) Matrix crystallization on the surface of bipolar-shell protected $CsPbI_3$ QDs. (F) Energy landscape of QD-in-matrix solids: charge carriers are funneled into QDs having a band gap smaller than that of the matrix, leading to photon emission.

increases, red-shifting spectra and changing the emission profile following extended photocarrier generation.[16]

Here, we report the epitaxial growth of a perovskite matrix onto perovskite QDs. We focus on the use of single-halide ($CsPbI_3$) perovskite QDs that enable epitaxial growth to form a homogeneous mixed-halide perovskite matrix. To enable the introduction of perovskite precursors on the QD surface, we develop a surface ligand treatment approach that introduces electrostatic stabilization of the perovskite QD using a dense iodide anion shell accompanied by a solvated cation shell (Figure 1D)[2]. Following surface treatment, the combination of the charged ionic ligand, and any remaining organic ligands, allows us to disperse QDs in a toluene/dimethylformamide (DMF) solvent mixture. We then introduce these into a perovskite precursor solution for spin-casting. The ligand-treated QDs retain their optoelectronic properties when dispersed in polar solvents saturated with low-dimensional mixed-halide perovskite precursors (PbX_2 and CsX in dimethyl sulfoxide (DMSO), details in Experimental Section, X = Br, I) during matrix growth (Figure 1E). We observe bright red emission after mixing QD and precursor solutions, indicating that the perovskite QDs remain intact during film fabrication (Supplementary Figure 1).

RESULTS AND DISCUSSION

To match the smaller lattice of the wider-band-gap Br/I perovskite matrix, we strained the $CsPbI_3$ QD by doping with small cations (Mn^{2+}) to induce lattice contraction.[17] To obtain a type-I band alignment with sufficient band offsets, we tuned the thickness of the mixed-halide perovskite matrix by introducing terminating ligands to induce quantum confinement. In this study, we construct red-emitting heterostructures composed of QDs with a size of ~4 nm, an optical band gap of ~1.9 eV, and a lattice constant ~ 6.03 Å and a matrix perovskite with ~40% Br, 5−8 nm thickness (Supplementary Figure 2), and a band gap of ~2.2 eV. In the QDs, strain induced by doping blue-shifts the luminescence spectrum.[18]

Figure 1A−C shows the formation of traditional low-dimensional mixed-halide perovskite solids made without QDs. When anti-solvent is added into precursors, supersaturation is rapidly achieved. Since the solubilities of perovskite precursors depend on the choice of halide, nuclei form that possess different halide concentrations, and these grow to form domains of different halide compositions. Elemental mapping confirms the uneven distribution of Br- and I- in the perovskite film (Supplementary Figure 3). Photoexcited charges are therefore spatially separated in domains with different halide compositions and sizes (Figure 1C). This compromises

https://doi.org/10.1021/jacs.1c02148
J. Am. Chem. Soc. XXXX, XXX, XXX−XXX

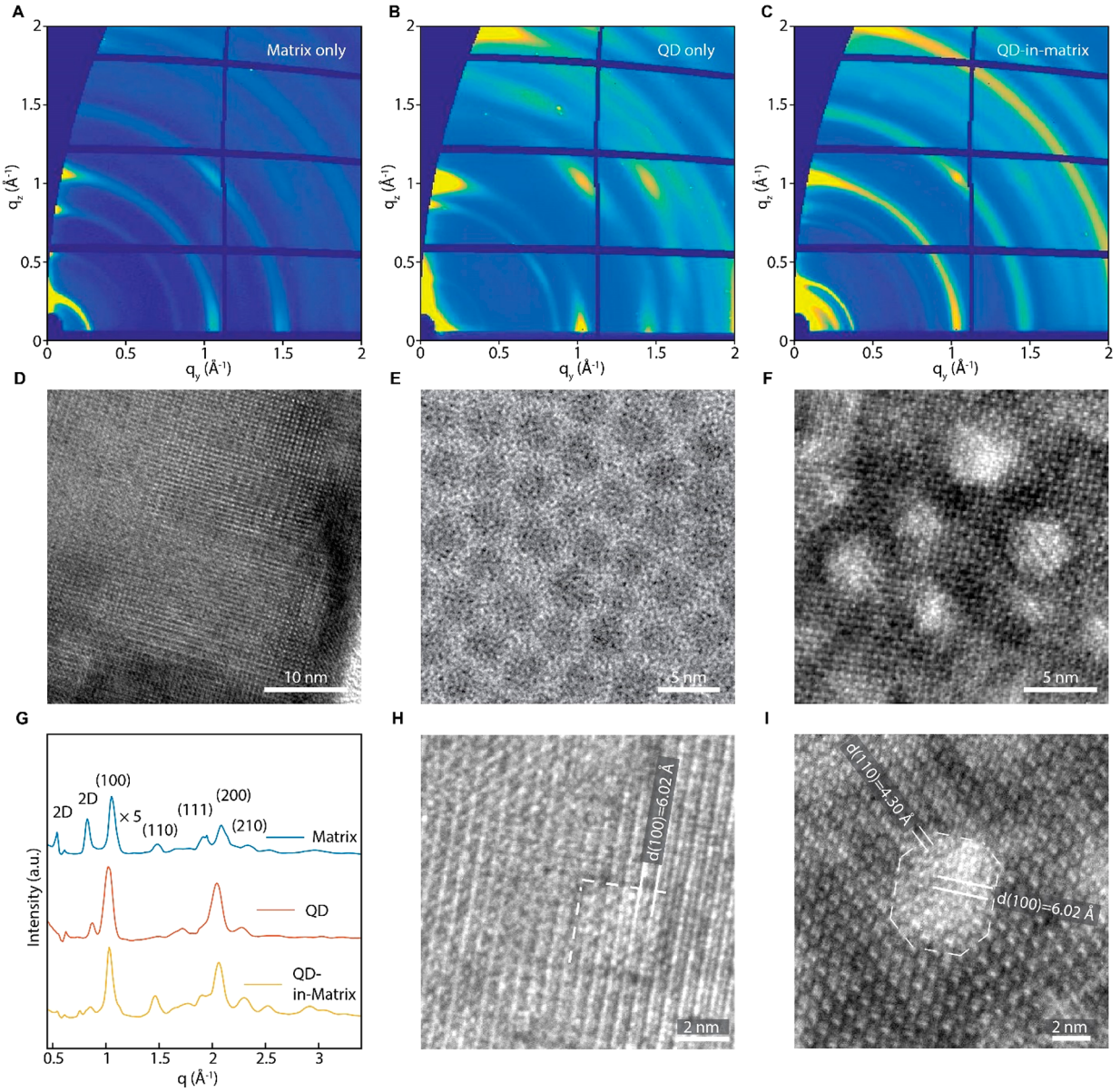

Figure 2. Structural characterization of QD-in-matrix solids. (A–C) GIWAXS diffraction patterns of (A) $CsPb(Br_xI_{1-x})_3$ matrix, (B) $CsPbI_3$ QD, and (C) QD-in-matrix solid. (D–F) HRTEM images of (D) $CsPb(Br_xI_{1-x})_3$ matrix, (E) $CsPbI_3$ QD, and (F) QD-in-matrix solid. (G) Azimuthally integrated scattering patterns of the materials. (H, I) HRTEM images reveal the *d*-spacing values of (100) and (110) planes at the QD-matrix interface.

luminescence efficiency and induces charge accumulation in the material.[18]

Small perovskite QDs serve as nucleation centers for perovskite growth; however, these QDs normally degrade in polar solvents required to dissolve perovskite precursors (Supplementary Figure 1). When QDs are treated with ionic ligands, electrostatic stabilization of QDs in small amounts of precursor solutions (see *in situ* photoluminescence (PL) studies of Supplementary Figure 1) facilitates crystal growth and works against gradient crystallization. Compared with crystal growth on nuclei having different halide compositions, growing perovskite on a predefined quantum dot with its chosen lattice constant (6.03 Å herein) favoring a specific composition (Br/I = ~4:6 herein) shows a more even halide distribution (Supplementary Figure 3) across crystal grains. This flattens the energy landscape within the matrix portion of the resultant materials system (Figure 1F). We find that the introduction of strain using Mn doping is necessary during material fabrication: undoped QDs degraded when mixed with precursor solution (Supplementary Figure 1).

Grazing-incidence wide-angle X-ray scattering (GIWAXS) diffraction patterns provide insight into the QD-assisted crystallization process. The diffraction pattern of mixed-halide matrix perovskite (Figure 2A) shows an orientational preference parallel to the substrate, a finding we attribute to thin perovskite quantum wells formed via nucleation assisted by solvated complexes.[19] Integrated GIWAXS patterns also reveal 2D perovskite structures ($PEA_2Cs_{n-1}Pb_n(I_{0.6}Br_{0.4})_{3n+1}$) (Figure 2G). In contrast, these structures are not observed in either $CsPbI_3$ QDs or QD-in-matrix films (Figure 2B,C). This suggests that the matrix grows more isotropically around QDs, a finding we explain by noting that 2D structures growing from small nuclei with random halide compositions will suffer more from inhomogeneous crystallization. These observations are

https://doi.org/10.1021/jacs.1c02148
J. Am. Chem. Soc. XXXX, XXX, XXX–XXX

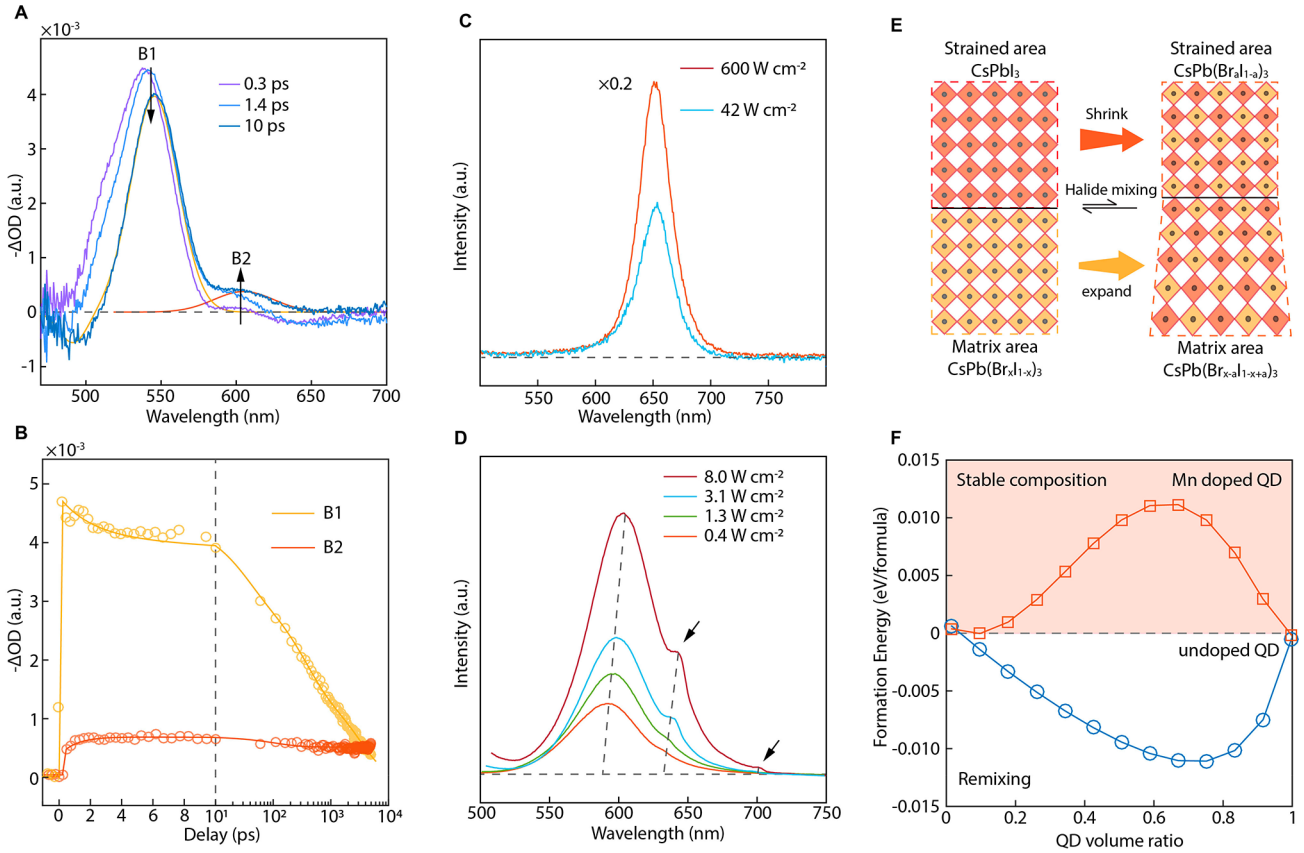

Figure 3. Optical properties of QD-in-matrix solids. (A) TA spectra of QD-in-matrix solid. (B) Kinetic traces of the B1 and B2 peaks of the QD-in-matrix solid. (C, D) Excitation-rate-dependent PL spectra of (C) QD-in-matrix solid and (D) $CsPb(Br_xI_{1-x})_3$ matrix. (E) Schematic of transition from compositionally stable QD-in-matrix phase to halide remixed phase where bromide migrates from matrix to strained QD. The exchange of anions with different atomic sizes between the QD/matrix interface induces strain in the material. (F) Total free energies change (red) of the transition illustrated in (E) as a function of strained QD volume ratio in the material. The free energy changes of the halide mixing process from a mixture of unstrained iodide domains and matrix perovskite with the same volume ratio to halide-remixed phase are also plotted (blue).

also verified in powder XRD measurements (Supplementary Figure 4). Additionally, the GIWAXS diffraction patterns of the QD-in-matrix are more intense than those of the matrix itself, indicating better crystallinity within perovskite in which QDs are embedded. The diffraction patterns in Figure 2G also show an agreement on lattice planes between QDs and matrix with only $a < 1\%$ peak position difference.

High-resolution transmission electron microscopy (HRTEM) images of the QD-in-perovskite matrix confirm its structure (Figure 2F). We account for the observed contrast in TEM by noting the distinct composition of QDs ($CsPbI_3$) compared to that of the matrix ($PEA_2Cs_{n-1}Pb_n(I_{0.6}Br_{0.4})_{3n+1}$). QDs with diameters ~ 4 nm are embedded in the mixed-halide perovskite matrix, whereas the perovskite matrix shows a featureless perovskite crystal (Figure 2D) and the QD film shows isolated QDs (Figure 2E). To ascertain whether QDs are inside the perovskite matrix, we obtained cross-sectional TEM images and *in situ* PL during film rinsing (Supplementary Figures 1, 6): QD-in-matrix film is homogeneous throughout the thickness dimension, and QDs remain after rinsing. Spacing differences are not observed between the core QDs and the mixed-halide perovskite matrix (HRTEM images; see Figure 2H,I), implying orientational alignment at the facets upon which growth occurs. Lattice fringes of 6.02 and 4.30 Å spacings are ascribed to (100) and (110) planes, respectively. Fast Fourier transform images further corroborate lattice match between the QDs and the matrix (Supplementary Figure 5). There is an absence of freestanding QDs in TEM images (Supplementary Figure 6); we conclude that the QDs function consistently as nucleation centers.

Embedded in a semiconducting matrix, the QDs act as luminophores and charge acceptors. The matrix perovskite without QDs has multiple PL emission peaks, a result of the different domains (650 and 700 nm). The QD-in-matrix materials exhibit PL arising from the QDs alone and show no discernible emission from the matrix (Figure 3C,D). We also fabricated QD-in-matrix structures using 3D formamidinium lead bromide/iodide ($FAPb(Br_xI_{1-x})_3$) perovskite as the matrix. Given that the lattice spacing of cubic FA perovskite is ~1.1% larger than that of the cesium perovskite, following the lattice matching requirement, we incorporate more Br^- into the matrix to shrink its lattice when growing mixed-halide FA perovskite onto QDs. The soft perovskite crystal structure may allow for lattice mismatch;[20] however, strongly confined perovskite QDs are known to be less defect tolerant than large ones, and there exists the possibility that a large mismatch may induce inhomogeneous crystallization. These hybrid materials also show PL only from the QDs, compared to matrix-only film fabricated using the same anti-solvent dripping method only in the absence of QDs, supporting the type-I interpretation (Supplementary Figure 7).

We investigated the optical properties of QD-in-matrix solids. Transient absorption (TA) spectra show two bleach peaks at ~550 nm (B1) and ~610 nm (B2) (Figure 3A). We

https://doi.org/10.1021/jacs.1c02148
J. Am. Chem. Soc. XXXX, XXX, XXX−XXX

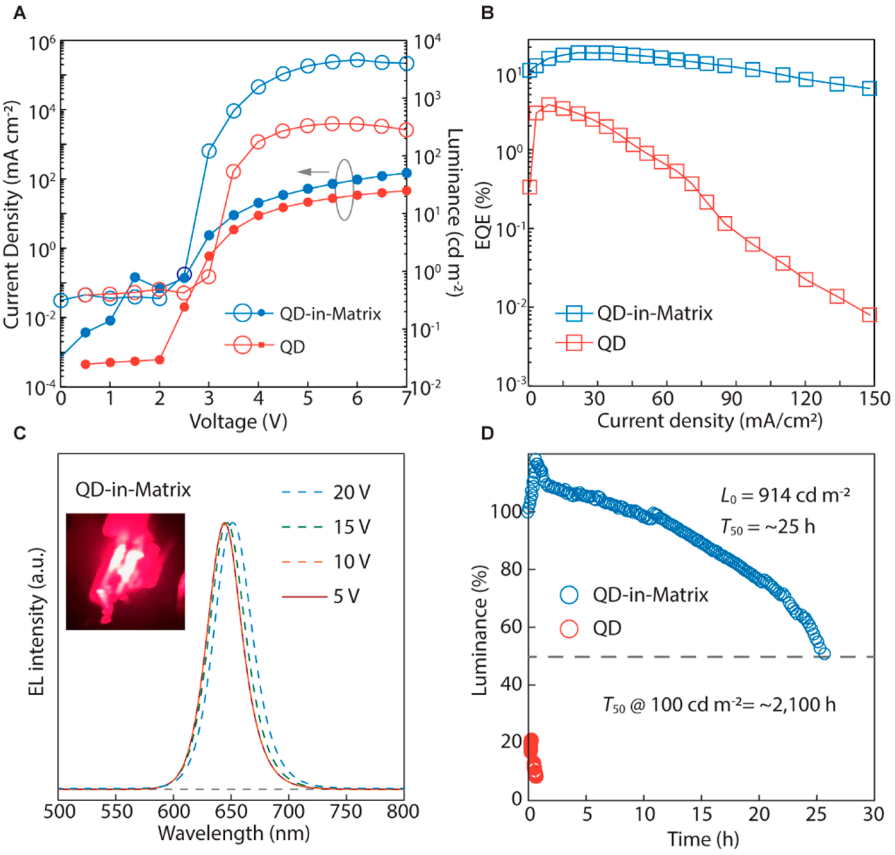

Figure 4. Electroluminescence and operating stability of LEDs. (A) Luminance and current density, as a function of applied bias, for QD and QD-in-matrix LEDs. (B) External quantum efficiency (EQE) as a function of current density for QD and QD-in-matrix LEDs. (C) Electroluminescence spectrum of a representative QD-in-matrix LED at different driving voltages. (D) Relative luminance versus operation time at ambient condition (23−25 °C; relative humidity ∼ 30%), measured with a constant drive current and an initial luminance of 914 cd m^{-2} (QD-in-matrix LED) and 184 cd m^{-2} (QD-only LED). The lifetime (T_{50}) of QD-in-matrix LED at 100 cd m^{-2} is estimated to be ∼2100 h based on an acceleration factor (n) of 1.95 (Supplementary Figure 16).

assign these to the band edge bleach of the matrix, and that of the QDs, respectively. The PL spectrum of the hybrid material shows no detectable emission from the perovskite matrix. The bleach recovery dynamics of B1 and B2 (Figure 3B) manifest fast recovery of B1 simultaneously with increasing bleach amplitude of B2 in the first 2 ps. TA spectra in Figure 3A also show population transfer from B1 to B2. Time-resolved PL measurements also agree well with TA dynamics. A noticeable (≤1 ns) rise of the PL signal monitored at the QD emission wavelength, followed by a slow radiative decay, is observed. Such features disappear in matrix-only perovskites (Supplementary Figure 8). This is consistent with rapid charge funneling through the matrix and subsequent charge injection into the embedded QDs, in agreement with prior reports of ultrafast charge transfer from perovskite matrixes to smaller-band-gap acceptors.[9] The longer recovery time of B2 indicates that the carriers injected into the QDs are robust against surface traps, a benefit of epitaxial perovskite passivation.

Previous reports modeled the halide mixing and phase segregation using density functional theory (DFT) and found that, without light excitation, remixing to a homogeneous halide distribution is favored and is driven by the entropy, which compensates for the increase in mixing enthalpy.[21] However, the structure of the QD-in-matrix remains stable without significant halide remixing at the QD/matrix interface. We applied an analogous model to study the suppression of halide remixing (see Experimental Section). We find that the QD has compressive lattice strain due to Mn doping and that this contributes to QD stability: it allows for lattice matching between the iodide-rich QD and mixed-halide matrix, and it works against halide mixing between the QD and the matrix. As illustrated in Figure 3E, moving the halides between the QD and the matrix compromises lattice matching. This source of strain provides an increase in the free energy of the mixed system, and this exceeds the entropic contribution (details in Experimental Section and Supplementary Figures 9, 10). We find that QDs remain stable against remixing for QD content above ∼15% relative to the total volume (Figure 3F). This is in good agreement with the real QD volumetric ratio (15−20%) in our QD-in-matrix material (see Experimental Section and Supplementary Figure 11).

It is important also to ensure that halide segregation is not enhanced under optical irradiation,[22] an effect previously ascribed to charge separation and polaron formation.[18,23] We tested the photostability of QDs-in-matrix by monitoring the PL following extended photoexcitation. QD-in-matrix films show no detectable PL shift or peak shape change (Figure 3C) following intense excitation for over 10 min. The PL quantum yield (PLQY) of the QD-in-matrix film remains high (>40%) at an excitation fluence of ∼600 W cm^{-2} (Supplementary Figure 12), whereas the control QD film is photodegraded or shows unmeasurable PLQY (<0.5%). In comparison, experiments performed on the mixed-halide matrix without embedded QDs show red-shifted PL as well as the emergence

https://doi.org/10.1021/jacs.1c02148
J. Am. Chem. Soc. XXXX, XXX, XXX−XXX

of two new peaks at 650 and 700 nm, which we assign to iodide-rich regions (PL at 650 nm) and pure iodide regions (PL at 700 nm) formed as a result of halide migration (Figure 3D). The narrow emission line width, and absence of low-energy emission peak, in the case of QD-in-matrix solids, also supports the picture that the QDs stabilize the matrix.

We fabricate LEDs using a device structure of ITO/poly[*N*,*N*′-bis(4-butylphenyl)-*N*,*N*′-bis(phenyl)-benzidine] (poly-TPD)/LiF/Perovskite/TPBi/LiF/Al. QDs without matrix protection degrade rapidly under high bias: QD-only LEDs exhibit a moderate luminance (~410 cd m^{-2}) at low bias (~5 V) and then experience a drop as bias is increased (Figure 4A).

Efficiency roll-off in QD LEDs happens due to surface degradation and nonradiative Auger recombination.[24] In QD-in-matrix solids, surfaces of QDs are protected by the matrix. Further, charges are partially delocalized into the matrix; thus, the overlap between the initial and final states involved in the Auger process is reduced.[25] Consequently, the bi-exciton Auger process of the QD-in-matrix solid is suppressed: its rate is ~10 times slower than that in QD-only samples (Supplementary Figure 13).

We observe a 12× higher maximum luminance (~4700 cd m^{-2}) and higher efficiency (~18%) in QD-in-matrix LEDs compared to the QD-only control (Figure 4A,B). The EQE remains ~13% even under high injection (100 mA cm^{-2}), while a severe droop in the QD-only LED was observed. No electroluminescence shift was observed in QD-in-matrix LEDs under a bias of 10 V; a slight (~5 nm) shift occurs under bias > 15 V (Figure 4C). The LEDs herein show a significant improvement in achieving simultaneous high brightness and high efficiency over reported solution-processed LEDs (Supplementary Figure 14).

We also find that the device performance is affected by scan rate (Supplementary Figure 15). We account for this dependence by noting ion motion in perovskite matrix materials.[26] To examine the matter in more detail, we examined the performance dependence of QD-in-matrix solids made using different sized QDs. We observed a larger scan rate dependence in the QD-in-matrix with small QDs than in the material using larger QDs. This is attributed to potentially more interfacial vacancies in QD-in-matrix solids with small QDs due to their increased surface area and high-index facets. This is in agreement with the observed small EL red shift after three scan cycles (Supplementary Figure 15). It is also worth noting that heat generated during slow scanning will also accelerate the ion migration and thus further contribute to the scan rate dependence of the device performance.

We examined the lifetime (T_{50}) of QD-in-matrix devices by measuring the luminance overtime at constant current densities (e.g., 20 mA cm^{-2}) (Figure 4D, Supplementary Figure 16). The QD-in-matrix structure ensured a QD surface that is much more stable than bare QDs.

An empirical equation (eq 1) is used to fit the results

$$L_0^n \times T_{50} = C \quad (1)$$

where L_0, n, and C are initial luminance, acceleration factor, and constant, respectively. Using the value of T_{50} measured at various initial luminance, the n value is determined to be 1.95 for QD-in-matrix LEDs (Supplementary Figure 16). The T_{50} at 100 cd m^{-2} is estimated to be 2100 h for QD-in-matrix LEDs, whereas the T_{50} of the QD-only device at ~184 cd m^{-2} is merely 25 min. This value is 2 orders of magnitude higher than the best previously reported values for primary red perovskite LEDs. To our knowledge, it is also the highest lifetime reported for perovskite-based visible LEDs (Supplementary Table 4). In addition to accelerated stability tests, we also investigated device hysteresis (Supplementary Figure 17) and the lifetime of QD-in-matrix devices at a lower initial luminance (~100 cd m^{-2}): we found no observable decay in brightness over 100 h (Supplementary Figure 18).

It is well-known that the interface of perovskite affects device operation stability.[27] In the device architecture mentioned above, the perovskite deposition using polar solvent is still less compatible with the nonpolar hole transport layer (HTL) compared with a polar HTL, despite the coating of a thin LiF layer.[28] This has the potential to result in more interfacial vacancy sites, thus compromising device stability. Therefore, we also tested the operating stability of the QD-in-matrix LEDs using polar PEDOT:PSS:PFI as HTL and obtained a larger T_{50} (~2400 h) (Supplementary Figure 19) with an n value of 2.16. It is also worth noting that the potentially accelerated ion migration at a large driving current will speed up the device degradation, thus leading to a slight overestimation of the n value.

The solution-processed QD-in-matrix materials that require polar solvent are more compatible with polar PEDOT:PSS:PFI HTL; however, the failure to block electrons limited the LED performance in this structure. Developing a stable and process compatible HTL remains an important future step.

CONCLUSIONS

Perovskite QD-in-matrix heteroepitaxial structures enable QD cores and mixed-halide perovskite matrixes that provide mutual stabilization. This leads to reduced gradient crystallization and suppressed halide segregation, and these enable charge carrier transport to the dots, leading to high-performance QD LEDs that unite high efficiency and high brightness with improved stability compared to prior perovskite reports.

EXPERIMENTAL SECTION

$CsPbI_3$ QD Synthesis and Purification. Strain-tuned $CsPbI_3$ QDs were synthesized and purified following previously reported methods by replacing the bromide precursor with their iodide counterparts.[1,29] 300 mg of Cs_2CO_3, 1.2 mL of oleic acid (OAc), and 3.2 mL of 1-octadecene (ODE) were loaded in a three-neck round-bottom flask under nitrogen and dried at room temperature for 10 min. Then the Cs-precursors were dissolved at 150 °C under a N_2 atmosphere. The solution was maintained above 100 °C before use.

While details can be found in the referred reports,[1,29] in brief, in a glovebox, 300 mg of $Mn(Ac)_2{\cdot}4H_2O$, 200 mg of PbI_2, and 360 mg of ZnI_2 were loaded in a 150 mL three-neck flask with 4 mL of OAc, 4 mL of oleylamine, and 8 mL of ODE. After stirring the solution in the flask for ~1 min, 300 μL of hydroiodic acid was added in the mixture and the mixture was stirred for another 3 min, followed by vacuum drying at 110 °C for 15 min. The precursor solution was heated to 170 °C under a N_2 atmosphere; then 0.8−0.9 mL of cesium precursor solution was swiftly injected into the flask. The reaction was kept at 170 °C for 1 min and quenched by an ice water bath. The obtained particles were precipitated by adding ~30 mL of methyl acetate, followed by centrifugation at 7800 rpm. The precipitants were redissolved in 5 mL of toluene and centrifuged at 7800 rpm to remove undissolved solids. The supernatant was then collected for storage.

Perovskite QD Surface Treatment. The QD solution was centrifuged again before surface treatment. The concentration of the QD solution was estimated by measuring the optical density of the solution at 500 nm. For each treatment, ~5 mL of solution with an OD of ~40 at 500 nm was used. Before ligand treatment, QDs were

https://doi.org/10.1021/jacs.1c02148
J. Am. Chem. Soc. XXXX, XXX, XXX−XXX

precipitated with methyl acetate one more time and dissolved into ~5 mL of toluene. Then ~0.1 mL of 250 mg/mL IPAI solution in DMF was added in the mixture.[2] The solution was vortexed and centrifuged at 7800 rpm for 30 s to remove any possible turbidity. The QDs were then reprecipitated by adding ~20 mL of methyl acetate, followed by redispersing in ~5 mL of toluene. The same procedure was repeated one more time using ~50 μL of IPAI solution to ensure a complete ligand treatment.

To maintain an iodine-rich surface for perovskite growing, ~50 μL of KI solution (200 mg/mL in DMF) was used for an additional ligand treatment iteration. The final ligand treated QD was dissolved in 1:9 DMF/toluene solution, followed by centrifuging at 15 000 rpm to remove any nonsoluble impurities. The solution was used immediately after surface ligand treatment.

Perovskite Quantum Well Matrix Precursor. Low-dimensional perovskite quantum well precursor solutions were prepared by dissolving $PbBr_2$, PbI_2, MAI, CsI, and PEAI in DMSO. In detail, for a 40% Br and 5−8 nm thick matrix, 0.4 mmol of $PbBr_2$, 0.2 mmol of PbI_2, 0.32 mmol of CsI, 0.08 mmol of MAI, and 0.4 mmol of PEAI were mixed and dissolved in 1.5 mL of DMSO in a nitrogen-filled glovebox with continuous stirring for 30 min. The quantum confinement and band gap of the obtained perovskite matrix were tuned by varying the PEAI/Pb ratio and Br/I ratio in the precursor solution. All solutions were filtrated by 0.45 μm PTFE filters before use.

Perovskite QD-in-Matrix Solid Fabrication and LED Fabrication. On a substrate, 200 μL aliquots of precursor solutions were spin-coated via a two-step process at 1000 rpm and 5000 rpm for 10 and 30 s, respectively. Various amounts (100−200 μL) of ligand-treated QD solution were dripped onto the spin-coated precursor solution at 25−27 s of the second step to obtain different QD/matrix ratios. For control (matrix-only) films, the same anti-solvent (without QD) was dripped onto the precursor solution. The film was annealed at 45−55 °C for 2 min and then moved to another hot plate to anneal further at 110 °C for 5−10 min.

For LED fabrication, ITO glass substrates (ITO thickness ~ 35 nm) were cleaned using deionized water, acetone, and 2-propanol ultrasonically and dried. The HTL was prepared by spin-coating (1500 rpm for 45 s) poly-TPD (American Dye Source) solution (4 mg/mL in chlorobenzene) onto the ITO substrate, followed by annealing at 150 °C for 30 min. 2.5 nm of LiF was afterward deposited onto the HTL in a thermal evaporating chamber under a high vacuum (10^{-7} Torr)

PEDOT:PSS (Clevios PVP AL 4083) solution was mixed with perfluorinated ionomer (PFI, Nafion) at a mass ratio of 1:0.99 under continuous stirring for 2 h, followed by filtration using a 0.45 μm polyvinylidene difluoride filter. Under ambient condition, the PEDOT:PSS-PFI mixture was spin-coated onto the ITO substrate using a two-step method (500 rpm for 10 s and then 4500 rpm for 90 s with an accelerating rate of 250 rpm/s). The PEDOT:PSS-PFI coated (~150 nm) substrates were then annealed at 170 °C for 15 min. The substrates were further dried under vacuum for an additional 20 min before use.

The substrates were then transferred into a nitrogen-filled glovebox for the QD-in-matrix solid film coating using the method above, followed by spin-coating a layer of polymethyl methacrylate for better charge injection balance (~1 nm, PMMA, 1 mg/mL dissolved in methyl acetate). Then 35 nm of TPBi, 1 nm of LiF, and 90 nm of Al were deposited in a thermal evaporating chamber under a high vacuum (10^{-7} Torr). Masks with an effective area of 0.09 cm^2 were applied during the evaporation of LiF and Al. The electrodes were protected by attaching a piece of scotch tape. For stability measurement over 24 h, devices were encapsulated using a cover glass and UV adhesive.

LED Performance Measurements. The J-L-V characterizations of LEDs were obtained under ambient conditions using a Keithley 647 source meter. The EL spectra were collected using a precalibrated fiber coupled spectrometer (QE-pro, Ocean Optics). The spectrometer is further calibrated with a radiometric calibrated light source (HL-3P-INT-CAL, OceanOptics). The LED testing system and data processing method were cross-checked using a commercial planar OLED (purchased from Lumtec. Corp., T_{70} > 10 000 h) with a reference system that is separately calibrated in a different lab (Supplementary Figure 20).

Optical Measurements. *In situ* PL measurements were performed in a glovebox. A fiber equipped with a collimator lens was placed above the substrate to collect PL under the excitation of a UV lamp (365 nm). The intensity-dependent PL spectra of the dots-in-matrix and matrix films were collected by a fiber coupled spectrometer (QE-Pro, Ocean Optics) under the excitation of a power-tunable diode laser (445 nm). The power of the excitation light was measured in free space by a power meter (Ophir).

PL spectra of QD-in-matrix films and bare matrix films were collected by a Horiba Fluorolog system coupled with a xenon lamp. The PL spectra were collected using an integrating sphere and a calibrated monochromator: single-photon-detector assembly.

X-ray Scattering Measurements. GIWAXS measurements were performed at the (7.3.3) beamline of the Advanced Light Source (ALS), Lawrence Berkeley National Laboratory. The wavelength of the X-ray beam was 1.24 Å. The scattering patterns were obtained at a photon-incident angle of 0.20° with respect to the sample plane. Samples were scanned in a helium environment to reduce air scattering. Exposure times were 30 s. The scattering patterns were recorded using a Pilatus 2M detector at a fixed distance of 277.674 mm. Calibration of the lengths in reciprocal space was done by using silver behenate. Samples for GIWAXS were spin-coated on glass substrates following the same spin-coating and annealing procedures mentioned above.

XRD patterns were obtain by a benchtop X-ray diffractometer (Miniflex, Rigaku). QDs were purified twice using methyl acetate before deposited and dried onto a substrate for XRD measurements.

TEM, STEM, and EDX Measurement. Samples for TEM imaging were prepared by using the same spin-coating and annealing method above onto a copper TEM grid attached on a glass substrate. Cross-sectional samples for TEM were prepared using a focused ion beam (FIB, Hitachi NB5000). The accelerating voltage of the ion beam was 40 kV, with a gradual decrease in the accelerating voltage to 2 kV as the sample thickness decreases. TEM and STEM were performed using a Hitachi HF-3300 S/TEM, operated at 300 kV. The EDX spectrum and mapping were obtained by a built-in Bruker EDX detector.

TA Measurements. TA spectra were recorded using a femtosecond (fs) pump-probe spectroscopy system. The fs laser pulses were produced by a regeneratively amplified Yb:KGW laser (Light Conversion, Pharos) at a 1 kHz repetition rate. The pump pulse was generated by passing through an optical parametric amplifier (OPA, Light Conversion Orpheus) and chopped, while the other portion of the fundamental beam was directed onto a sapphire crystal after focusing to generate a white-light supercontinuum as the probe light. The power of the pump light was measured using a power meter (Ophir) to ensure excitation fluence is below the Auger threshold. The time delay of the probe pulses was optically controlled by a translation stage. The probe light spectra were collected with a CCD detector. TA bleach recovery dynamics were recorded at the band edge bleach peak position. The curve was fit with a multi-exponential decay function.

DFT Calculations. Mixed halide perovskite ($CsPb(Br_xI_{1-x})_3$ in orthorhombic (space group *Pnma*)) is modeled as a statistical ensemble of independent configurations for 13 compositions: x = 0, 1/12, 2/12, ..., 11/12, 1. The thermodynamics of the alloy was described by the generalized quasi-chemical approximation.[30,31] The following equation was used to evaluate the Helmholtz free energy

$$\Delta F(x,T) = \Delta U(x,T) - T\Delta S(x,T) \quad (2)$$

where $\Delta U(x,T)$ is the internal energy of the alloy, and $\Delta S(x,T)$ is the configurational entropy. To obtain these terms, the total energy E_i of each independent configuration (i) is calculated by DFT. The total number of configurations for this system is 2^{12} = 4096 (20 atoms in the unit cell, including 12 halide atoms). There were 592 independent configurations calculated by using the SOD code.[32] All DFT

https://doi.org/10.1021/jacs.1c02148
J. Am. Chem. Soc. XXXX, XXX, XXX−XXX

calculations were performed using the FHI-aims[33−35] all-electron code. The default numerical settings, referred to as "intermediate" in FHI-aims, were used. Local minimum-energy geometries of the Born−Oppenheimer surface were obtained with residual total energy gradients below 1×10^{-2} eV/Å for atomic positions using the PBE-GGA functional within the vdW correction following the TS approach (PBE+TS). A $6 \times 4 \times 6$ Γ-point centered k-space mesh was used for all configurations. The $\Delta U(x,T)$, $\Delta S(x,T)$, and $\Delta F(x,T)$ of the $CsPb(Br_xI_{1-x})_3$ alloy are shown in Supplementary Figure 9.

Using the initial composition of the matrix ($CsPb(Br_{0.4}I_{0.6})_3$) used in this work, Supplementary Figure 10 shows the calculated $\Delta F_{mix}(x,300\ K)$ as the halide mixing energy by using the equation:

$$\Delta F_{mix}(x,300) = \Delta F(x,300) - CsPbI_3\%\Delta F(0,300) - Matrix\%\Delta F(0.4,300) \quad (3)$$

where $CsPbI_3$% and Matrix% represents the molar ratio of $CsPbI_3$ domains and the matrix in the hybrid material, respectively. A negative ΔF_{mix} indicates that, in perovskites consisting of unstrained $CsPbI_3$ domains (same size and composition with QD) and the $CsPb(Br_{0.4}I_{0.6})_3$ matrix, bromide anions tend to migrate into the $CsPbI_3$ region, forming a homogeneous halide composition ($CsPb(Br_xI_{1-x})_3$, $x < 0.4$).

QDs used in this work possess local strain induced by immobilized small ionic dopants (Mn^{2+}). The local strain will transport via the perovskite lattice within the "coherence length" in which the matrix around the QDs is also experiencing the strain. If halide mixing happened across the QD/matrix interface, the already strained lattice in the matrix near QDs will have to expand due to higher iodide concentration. As a result, the free energy of the system will increase. To calculate the free energy change of the halide mixing process described in eq 3 in the strained QD-in-matrix system, the following equation is used:

$$\Delta F_{mix(QD\text{-}in\text{-}matrix)}(x,300) = QD\%\Delta F_{(strained\ QD)}(x,300) + Matrix\%\Delta F_{(strained\ matrix)}(x,300) + \Delta F_{mix}(x,300) \quad (4)$$

where $\Delta F_{(strained\ QD)}$ and $\Delta F_{(strained\ matrix)}$ represent the strain-induced free energy increase of the QD and matrix after halide mixing, respectively.

$\Delta F_{(strained\ QD)}$ is calculated based on four different remix compositions ($CsPb(Br_xI_{1-x})_3$, x = 1/12, 2/12, 3/12, 4/12) while QDs comprise $CsPbI_3$ only and the matrix is $CsPb(Br_{0.4}I_{0.6})_3$. The crystal structures for the above-mentioned four compositions are based on the most stable configurations (lowest total energies) from the previous Helmholtz free energy calculations. From the synchrotron X-ray data, the degree of strain is estimated to be ∼ −3% upon the one-dimensional lattice. The same extent of strain is applied to QDs with composition $CsPb(Br_xI_{1-x})_3$ after halide mixing. To calculate the total energy of the strained QDs, lattice vectors of the PBE+TS relaxed structures for QD are constrained to lattice volume reduced by ∼3% of its unstrained counterpart.

The calculated $\Delta F_{(strained\ QD)}$ is listed in Supplementary Table 1 for the above-mentioned four different compositions. The values of $\Delta F_{(strained\ QD)}$ is independent of composition. Therefore, the average value of 0.011 eV/formula was used in all calculations below.

$\Delta F_{(strained\ matrix)}$ is also calculated for the same four compositions above. To simplify the calculation, the strain effect in the matrix was averaged by assuming the strain in the QD region was transferred throughout the entire volume of the matrix. This may slightly overestimate or underestimate the strain effect in different matrix areas though; we are still able to evaluate the overall trend of energy changes in this material. Therefore, the strain applied in the matrix is $-3\% \times V(QD)/(V(QD) + V(Matrix)) = -3\% \times QD\%$. Using the same method above, the value of $\Delta F_{(strained\ matrix)}$ is calculated and listed in Supplementary Table 2.

The values of $\Delta F_{(strained\ matrix)}$ are composition-dependent and were fit into a polynomial function ($y = 0.1416(Matrix\%)^2 - 0.2893 Matrix\% + 0.1484$).

On the basis of eq 4, the $\Delta F_{mix(QD\text{-}in\text{-}matrix)}$ values were calculated for a series of x values and the x values were transferred to QD volume ratios as plotted in Figure 3F. The "coherence length (l)" was estimated by

$$l = \left(\sqrt[3]{\frac{1}{QD\%}} - 1\right) \times r \quad (5)$$

where QD% is the volume ratio of QD when $\Delta F_{mix(QD\text{-}in\text{-}matrix)}$ is zero and r is the radius of the QD. For r = 2−2.5 nm, l = 1.7−2.0 nm. This is in good agreement of half of the inter-QD distance measured from TEM images. Supplementary Figure 11 shows the histogram plot of ∼150 interparticle distance values measured from TEM images.

■ ASSOCIATED CONTENT

Supporting Information

The Supporting Information is available free of charge at https://pubs.acs.org/doi/10.1021/jacs.1c02148.

Materials, Supplementary Figures 1−20, and Supplementary Tables 1−4 (PDF)

■ AUTHOR INFORMATION

Corresponding Author

Edward H. Sargent − *Department of Electrical and Computer Engineering, University of Toronto, Toronto, Ontario M5S 1A4, Canada;* orcid.org/0000-0003-0396-6495; Email: ted.sargent@utoronto.ca

Authors

Yuan Liu − *Department of Electrical and Computer Engineering, University of Toronto, Toronto, Ontario M5S 1A4, Canada;* orcid.org/0000-0001-8611-1673

Yitong Dong − *Department of Electrical and Computer Engineering, University of Toronto, Toronto, Ontario M5S 1A4, Canada*

Tong Zhu − *Department of Electrical and Computer Engineering, University of Toronto, Toronto, Ontario M5S 1A4, Canada*

Dongxin Ma − *Department of Electrical and Computer Engineering, University of Toronto, Toronto, Ontario M5S 1A4, Canada;* orcid.org/0000-0002-9790-5951

Andrew Proppe − *Department of Electrical and Computer Engineering, University of Toronto, Toronto, Ontario M5S 1A4, Canada; Department of Chemistry, University of Toronto, Toronto, Ontario M5S 3G4, Canada*

Bin Chen − *Department of Electrical and Computer Engineering, University of Toronto, Toronto, Ontario M5S 1A4, Canada*

Chao Zheng − *Department of Electrical and Computer Engineering, University of Toronto, Toronto, Ontario M5S 1A4, Canada*

Yi Hou − *Department of Electrical and Computer Engineering, University of Toronto, Toronto, Ontario M5S 1A4, Canada*

Seungjin Lee − *Department of Electrical and Computer Engineering, University of Toronto, Toronto, Ontario M5S 1A4, Canada;* orcid.org/0000-0002-6318-0702

Bin Sun − *Department of Electrical and Computer Engineering, University of Toronto, Toronto, Ontario M5S 1A4, Canada;* orcid.org/0000-0002-8233-0999

https://doi.org/10.1021/jacs.1c02148
J. Am. Chem. Soc. XXXX, XXX, XXX−XXX

Eui Hyuk Jung − *Department of Electrical and Computer Engineering, University of Toronto, Toronto, Ontario M5S 1A4, Canada;* orcid.org/0000-0002-2833-522X
Fanglong Yuan − *Department of Electrical and Computer Engineering, University of Toronto, Toronto, Ontario M5S 1A4, Canada; Department of Materials Science and Engineering, University of Toronto, Toronto, Ontario M5S 3E4, Canada*
Ya-kun Wang − *Department of Electrical and Computer Engineering, University of Toronto, Toronto, Ontario M5S 1A4, Canada*
Laxmi Kishore Sagar − *Department of Electrical and Computer Engineering, University of Toronto, Toronto, Ontario M5S 1A4, Canada;* orcid.org/0000-0002-7656-7308
Sjoerd Hoogland − *Department of Electrical and Computer Engineering, University of Toronto, Toronto, Ontario M5S 1A4, Canada;* orcid.org/0000-0002-3099-585X
F. Pelayo García de Arquer − *Department of Electrical and Computer Engineering, University of Toronto, Toronto, Ontario M5S 1A4, Canada; Department of Chemistry, University of Toronto, Toronto, Ontario M5S 3G4, Canada;* orcid.org/0000-0003-2422-6234
Min-Jae Choi − *Department of Electrical and Computer Engineering, University of Toronto, Toronto, Ontario M5S 1A4, Canada;* Present Address: Department of Chemical and Biochemical Engineering, Dongguk University, Seoul 04620, Republic of Korea
Kamalpreet Singh − *Department of Physical and Environmental Sciences, University of Toronto, Toronto, Ontario M1C 1A4, Canada;* orcid.org/0000-0001-8569-1119
Shana O. Kelley − *Department of Chemistry, University of Toronto, Toronto, Ontario M5S 3G4, Canada;* orcid.org/0000-0003-3360-5359
Oleksandr Voznyy − *Department of Physical and Environmental Sciences, University of Toronto, Toronto, Ontario M1C 1A4, Canada;* orcid.org/0000-0002-8656-5074
Zheng-Hong Lu − *Department of Materials Science and Engineering, University of Toronto, Toronto, Ontario M5S 3E4, Canada;* orcid.org/0000-0003-2050-0822

Complete contact information is available at: https://pubs.acs.org/10.1021/jacs.1c02148

Author Contributions

[⊥]These authors contributed equally.

Notes

The authors declare no competing financial interest.

■ ACKNOWLEDGMENTS

This work was supported by the Natural Sciences and Engineering Research Council of Canada (NSERC, grant number 537463-18). The authors acknowledge Huawei Canada for their financial support. Z.-H.L. and all co-authors from the Department of Materials Science and Engineering at the University of Toronto acknowledge the financial support from the Natural Sciences and Engineering Research Council of Canada (NSERC, grant number 216956-12), and the National Natural Science Foundation of China (grant number 11774304). Electron microscopy was performed at the Ontario Centre for the Characterization of Advanced Materials, funded by the Canada Foundation for Innovation (CFI).

■ REFERENCES

(1) Dong, Y.; Qiao, T.; Kim, D.; Parobek, D.; Rossi, D.; Son, D. H. Precise Control of Quantum Confinement in Cesium Lead Halide Perovskite Quantum Dots via Thermodynamic Equilibrium. *Nano Lett.* **2018**, *18* (6), 3716−3722.
(2) Dong, Y.; Wang, Y.-K.; Yuan, F.; Johnston, A.; Liu, Y.; Ma, D.; Choi, M.-J.; Chen, B.; Chekini, M.; Baek, S.-W.; Sagar, L. K.; Fan, J.; Hou, Y.; Wu, M.; Lee, S.; Sun, B.; Hoogland, S.; Quintero-Bermudez, R.; Ebe, H.; Todorovic, P.; Dinic, F.; Li, P.; Kung, H. T.; Saidaminov, M. I.; Kumacheva, E.; Spiecker, E.; Liao, L.-S.; Voznyy, O.; Lu, Z.-H.; Sargent, E. H. Bipolar-Shell Resurfacing for Blue LEDs Based on Strongly Confined Perovskite Quantum Dots. *Nat. Nanotechnol.* **2020**, *15* (8), 668−674.
(3) Chiba, T.; Hayashi, Y.; Ebe, H.; Hoshi, K.; Sato, J.; Sato, S.; Pu, Y.-J. J.; Ohisa, S.; Kido, J. Anion-Exchange Red Perovskite Quantum Dots with Ammonium Iodine Salts for Highly Efficient Light-Emitting Devices. *Nat. Photonics* **2018**, *12* (11), 681−687.
(4) Kim, Y.-H.; Kim, S.; Kakekhani, A.; Park, J.; Park, J.; Lee, Y.-H.; Xu, H.; Nagane, S.; Wexler, R. B.; Kim, D.-H.; Jo, S. H.; Martínez-Sarti, L.; Tan, P.; Sadhanala, A.; Park, G.-S.; Kim, Y.-W.; Hu, B.; Bolink, H. J.; Yoo, S.; Friend, R. H.; Rappe, A. M.; Lee, T.-W. Comprehensive Defect Suppression in Perovskite Nanocrystals for High-Efficiency Light-Emitting Diodes. *Nat. Photonics* **2021**, *15* (2), 148−155.
(5) Anderson, N. C.; Hendricks, M. P.; Choi, J. J.; Owen, J. S. Ligand Exchange and the Stoichiometry of Metal Chalcogenide Nanocrystals: Spectroscopic Observation of Facile Metal-Carboxylate Displacement and Binding. *J. Am. Chem. Soc.* **2013**, *135* (49), 18536−18548.
(6) Kagan, C. R.; Murray, C. B. Charge Transport in Strongly Coupled Quantum Dot Solids. *Nat. Nanotechnol.* **2015**, *10* (12), 1013−1026.
(7) Chen, O.; Zhao, J.; Chauhan, V. P.; Cui, J.; Wong, C.; Harris, D. K.; Wei, H.; Han, H. S.; Fukumura, D.; Jain, R. K.; Bawendi, M. G. Compact High-Quality CdSe-CdS Core-Shell Nanocrystals with Narrow Emission Linewidths and Suppressed Blinking. *Nat. Mater.* **2013**, *12* (5), 445−451.
(8) Li, Y.; Hou, X.; Dai, X.; Yao, Z.; Lv, L.; Jin, Y.; Peng, X. Stoichiometry-Controlled InP-Based Quantum Dots: Synthesis, Photoluminescence, and Electroluminescence. *J. Am. Chem. Soc.* **2019**, *141* (16), 6448−6452.
(9) Ning, Z.; Gong, X.; Comin, R.; Walters, G.; Fan, F.; Voznyy, O.; Yassitepe, E.; Buin, A.; Hoogland, S.; Sargent, E. H. Quantum-Dot-in-Perovskite Solids. *Nature* **2015**, *523* (7560), 324−328.
(10) Kovalenko, M. V.; Protesescu, L.; Bodnarchuk, M. I. Properties and Potential Optoelectronic Applications of Lead Halide Perovskite Nanocrystals. *Science* **2017**, *358* (6364), 745−750.
(11) De Roo, J.; Ibáñez, M.; Geiregat, P.; Nedelcu, G.; Walravens, W.; Maes, J.; Martins, J. C.; Van Driessche, I.; Kovalenko, M. V.; Hens, Z. Highly Dynamic Ligand Binding and Light Absorption Coefficient of Cesium Lead Bromide Perovskite Nanocrystals. *ACS Nano* **2016**, *10* (2), 2071−2081.
(12) Zhong, Q.; Cao, M.; Hu, H.; Yang, D.; Chen, M.; Li, P.; Wu, L.; Zhang, Q. One-Pot Synthesis of Highly Stable $CsPbBr_3$@SiO_2 Core-Shell Nanoparticles. *ACS Nano* **2018**, *12* (8), 8579−8587.
(13) Quan, L. N.; Quintero-Bermudez, R.; Voznyy, O.; Walters, G.; Jain, A.; Fan, J. Z.; Zheng, X.; Yang, Z.; Sargent, E. H. Highly Emissive Green Perovskite Nanocrystals in a Solid State Crystalline Matrix. *Adv. Mater.* **2017**, *29* (21), 1605945.
(14) Shi, E.; Yuan, B.; Shiring, S. B.; Gao, Y.; Akriti; Guo, Y.; Su, C.; Lai, M.; Yang, P.; Kong, J.; Savoie, B. M.; Yu, Y.; Dou, L. Two-Dimensional Halide Perovskite Lateral Epitaxial Heterostructures. *Nature* **2020**, *580* (7805), 614−620.
(15) Nedelcu, G.; Protesescu, L.; Yakunin, S.; Bodnarchuk, M. I.; Grotevent, M. J.; Kovalenko, M. V. Fast Anion-Exchange in Highly

Luminescent Nanocrystals of Cesium Lead Halide Perovskites ($CsPbX_3$, X = Cl, Br, I). *Nano Lett.* **2015**, *15* (8), 5635−5640.
(16) Brennan, M. C.; Draguta, S.; Kamat, P. V.; Kuno, M. Light-Induced Anion Phase Segregation in Mixed Halide Perovskites. *ACS Energy Lett.* **2018**, *3* (1), 204−213.
(17) Akkerman, Q. A.; Meggiolaro, D.; Dang, Z.; De Angelis, F.; Manna, L. Fluorescent Alloy $CsPb_xMn_{1-x}I_3$ Perovskite Nanocrystals with High Structural and Optical Stability. *ACS Energy Lett.* **2017**, *2* (9), 2183−2186.
(18) Draguta, S.; Sharia, O.; Yoon, S. J.; Brennan, M. C.; Morozov, Y. V.; Manser, J. S.; Kamat, P. V.; Schneider, W. F.; Kuno, M. Rationalizing the Light-Induced Phase Separation of Mixed Halide Organic-Inorganic Perovskites. *Nat. Commun.* **2017**, *8* (1), 200.
(19) Quintero-Bermudez, R.; Gold-Parker, A.; Proppe, A. H.; Munir, R.; Yang, Z.; Kelley, S. O.; Amassian, A.; Toney, M. F.; Sargent, E. H. Compositional and Orientational Control in Metal Halide Perovskites of Reduced Dimensionality. *Nat. Mater.* **2018**, *17* (10), 900−907.
(20) Stoumpos, C. C.; Kanatzidis, M. G. The Renaissance of Halide Perovskites and Their Evolution as Emerging Semiconductors. *Acc. Chem. Res.* **2015**, *48* (10), 2791−2802.
(21) Zhang, H.; Fu, X.; Tang, Y.; Wang, H.; Zhang, C.; Yu, W. W.; Wang, X.; Zhang, Y.; Xiao, M. Phase Segregation Due to Ion Migration in All-Inorganic Mixed-Halide Perovskite Nanocrystals. *Nat. Commun.* **2019**, *10* (1), 1088.
(22) Samu, G. F.; Janáky, C.; Kamat, P. V. A Victim of Halide Ion Segregation. How Light Soaking Affects Solar Cell Performance of Mixed Halide Lead Perovskites. *ACS Energy Lett.* **2017**, *2* (8), 1860−1861.
(23) Bischak, C. G.; Hetherington, C. L.; Wu, H.; Aloni, S.; Ogletree, D. F.; Limmer, D. T.; Ginsberg, N. S. Origin of Reversible Photoinduced Phase Separation in Hybrid Perovskites. *Nano Lett.* **2017**, *17* (2), 1028−1033.
(24) Lim, J.; Park, Y.-S. S.; Wu, K.; Yun, H. J.; Klimov, V. I. Droop-Free Colloidal Quantum Dot Light-Emitting Diodes. *Nano Lett.* **2018**, *18* (10), 6645−6653.
(25) Cragg, G. E.; Efros, A. L. Suppression of Auger Processes in Confined Structures. *Nano Lett.* **2010**, *10* (1), 313−317.
(26) Tress, W.; Marinova, N.; Moehl, T.; Zakeeruddin, S. M.; Nazeeruddin, M. K.; Grätzel, M. Understanding the Rate-Dependent J-V Hysteresis, Slow Time Component, and Aging in CH 3 NH 3 PbI 3 Perovskite Solar Cells: The Role of a Compensated Electric Field. *Energy Environ. Sci.* **2015**, *8* (3), 995−1004.
(27) Han, T.-H.; Tan, S.; Xue, J.; Meng, L.; Lee, J.-W.; Yang, Y. Interface and Defect Engineering for Metal Halide Perovskite Optoelectronic Devices. *Adv. Mater.* **2019**, *31*, 1803515.
(28) Zhao, B.; Lian, Y.; Cui, L.; Divitini, G.; Kusch, G.; Ruggeri, E.; Auras, F.; Li, W.; Yang, D.; Zhu, B.; Oliver, R. A.; MacManus-Driscoll, J. L.; Stranks, S. D.; Di, D.; Friend, R. H. Efficient Light-Emitting Diodes from Mixed-Dimensional Perovskites on a Fluoride Interface. *Nat. Electron.* **2020**, *3*, 704−710.
(29) Parobek, D.; Dong, Y.; Qiao, T.; Son, D. H. Direct Hot-Injection Synthesis of Mn-Doped $CsPbBr_3$ Nanocrystals. *Chem. Mater.* **2018**, *30* (9), 2939−2944.
(30) Sher, A.; Van Schilfgaarde, M.; Chen, A. B.; Chen, W. Quasichemical Approximation in Binary Alloys. *Phys. Rev. B: Condens. Matter Mater. Phys.* **1987**, *36* (8), 4279−4295.
(31) Brivio, F.; Caetano, C.; Walsh, A. Thermodynamic Origin of Photoinstability in the $CH_3NH_3Pb(I_{1-x}Br_x)_3$ Hybrid Halide Perovskite Alloy. *J. Phys. Chem. Lett.* **2016**, *7* (6), 1083−1087.
(32) Grau-Crespo, R.; Hamad, S.; Catlow, C. R. A.; de Leeuw, N. H. Symmetry-Adapted Configurational Modelling of Fractional Site Occupancy in Solids. *J. Phys.: Condens. Matter* **2007**, *19* (25), 256201.
(33) Blum, V.; Gehrke, R.; Hanke, F.; Havu, P.; Havu, V.; Ren, X.; Reuter, K.; Scheffler, M. Ab Initio Molecular Simulations with Numeric Atom-Centered Orbitals. *Comput. Phys. Commun.* **2009**, *180* (11), 2175−2196.
(34) Havu, V.; Blum, V.; Havu, P.; Scheffler, M. Efficient O (N) Integration for All-Electron Electronic Structure Calculation Using Numeric Basis Functions. *J. Comput. Phys.* **2009**, *228* (22), 8367−8379.
(35) Ren, X.; Rinke, P.; Blum, V.; Wieferink, J.; Tkatchenko, A.; Sanfilippo, A.; Reuter, K.; Scheffler, M. Resolution-of-Identity Approach to Hartree-Fock, Hybrid Density Functionals, RPA, MP2 and GW with Numeric Atom-Centered Orbital Basis Functions. *New J. Phys.* **2012**, *14* (5), 053020.

https://doi.org/10.1021/jacs.1c02148
J. Am. Chem. Soc. XXXX, XXX, XXX−XXX